Research Article

Thermal Parameters Inversion Method for Concrete Dam Based on Optimal Temperature Measuring Point Selecting

Fang Wang [ID],[1] Huawei Zhou,[1] Yihong Zhou [ID],[1] Chunju Zhao,[1] Ebrahim Aman Seman,[1] and Pan Gong[2]

[1]*China Three Gorges University, Hubei Key Laboratory of Construction and Management in Hydropower Engineering, Yichang 443002, China*
[2]*China Three Gorges Projects Development Corporation Limited, Chengdu 610041, China*

Correspondence should be addressed to Yihong Zhou; zyhwhu2003@163.com

Concrete thermal parameters in a natural pouring environment are essential inputs for simulating the temperature field of a concrete dam. This paper proposes a two-stage thermal parameters inversion method for a concrete dam based on optimal temperature measuring point selection to improve the accuracy of parameters. Firstly, a selection method of optimal measuring point for thermal parameters inversion is presented and the temperature response sensitivity of measuring points when the parameters disturb is taken as the critical evaluation index. And then, an inversion model is established based on support vector regression (SVR) and particle swarm optimization (PSO). Finally, the proposed method is applied to the thermal parameter inversion of a concrete dam. The results show that the proposed method is effective for improving the inversion accuracy and obtaining accurate parameters. The average error of the inversion results based on the SVR-PSO model is 28.54% lower than that of the genetic algorithm optimization using a back propagation neural network (BPNN-GA). Besides that, the average error of the inversion results based on the optimal measurement points is 35.57% lower than that of the nonoptimized ones.

1. Introduction

Temperature control and crack prevention are some of the key technologies for concrete dam construction [1]. The large size of the pouring block makes it difficult for the heat from the young concrete to dissipate, resulting in an apparent temperature difference near the heat dissipation boundary. Additionally, the old concrete is strongly constrained by the adjacent layers or the dam foundation. These two factors may cause some adverse temperature stress within the structure. When this temperature stress exceeds the concrete's tensile strength, cracks will occur [2]. Cracks will directly affect the construction quality, construction progress, and structural safety of the dam. It effectively reduces the cracking risk by simulating the temperature field in the construction period of concrete dams and obtaining the appropriate temperature control scheme [3].

In order to obtain the temperature field of concrete dam, scholars have proposed many calculation models based on the finite element method (FEM) [4–10]. Above studies focus on the improvement of the calculation model, theory, and method of temperature field during the construction period of concrete dams, which improves the calculation efficiency and the accuracy of calculation results. However, the reliability of temperature field simulation results is not only related to the algorithm model but also depends on the accuracy of thermal parameters [11]. Generally, the thermal parameters of concrete refer to similar projects or laboratory test data, which are affected by the batch of raw materials and environmental conditions. However, in a real pouring environment, the thermal parameters differ greatly from those derived by the above methods [12]. According to the monitoring data on the construction site, some scholars use inversion method to calculate the thermal parameters, which improves the accuracy of the parameters.

Inversion is a method for solving the model or its parameters of a system through measurable physical quantities. It is widely used in dam deformation analysis [13, 14] and seepage analysis [15]. The inversion problem of the temperature field of a dam is mainly related to solving the concrete thermal parameters based on the measured temperature. The inversion methods can be divided into analytical and iterative methods. The analytical method involves simplifying the concrete heat transfer problem to obtain an analytical expression between the inversion parameters and the monitored temperature, and then obtaining the temperature data to complete the inversion. This method is only suitable for parameter identification in a one-dimensional (1D) heat transfer problem [16], which makes its application range limited. The iterative method transforms the parameter solving problem into the optimization problem by gradually modifying the parameter value until approaching the optimal value. This method is easy to operate with a wide range of applications, and has become the main method of concrete thermal parameter inversion.

In recent years, the iterative inversion method for the thermal parameters of a concrete dam has developed rapidly. Ding and Chen [17] combined the precise algorithm for calculating a temperature field and the GA for solving an inverse problem and inversed the concrete thermal parameters according to the measured temperature data at the construction site. In order to improve the inversion accuracy, Chen and Yang [18] used the improved GA and the FEM to carry out an inversion analysis according to the concrete temperature observation data for a concrete dam. Pei et al. [19] combined a response surface model and a genetic algorithm to determine the concrete thermal parameters according to the internal temperature data of a dam, which improved the computational efficiency. Zhou et al. [20] first used the dam monitoring temperature and FEM to obtain the datasets, and then used BPNN to establish a mapping model between thermal parameters and concrete temperature. Finally, GA was used to invoke the trained neural network model to obtain the thermal parameters. Ouyang et al. [21] used the Levenberg-Marquardt algorithm to invert the thermal parameters of concrete based on the temperature data of a reservoir inlet tower. Wang et al. [22] used an improved PSO for concrete thermal parameter identification based on the internal temperature monitoring data of a concrete dam and verified it. A number of existing studies have focused on the selection and improvement of the optimization algorithm, and the accuracy and efficiency of inversion have been improved. In addition, the location of temperature measurement points is also one of the important influencing factors of the inversion.

Due to the large thermal resistance of concrete, the temperature response caused by some external disturbances [23], such as air temperature and water pipe cooling, is only in a limited space range, which means that the temperature response will gradually decay in this range. Moreover, measurement error is inevitable in the actual temperature monitoring of the pouring block. These results in that when the observed temperature response is small to a certain extent, the measurement error may be larger than the temperature response and overwhelm it. As a result, based on such temperature monitoring information, the thermal parameters obtained by inversion are often inaccurate. The traditional temperature control mode focuses on the variation of the average temperature inside the casting block [24], and the average temperature monitoring information from a few internal thermometers is sufficient for the inversion accuracy. It can be seen that the influence of temperature measurement point location is not significant, and relevant research rarely has been conducted. However, under the current background of refining temperature control of the concrete dam, besides the average internal temperature, the temperature variation in other parts, such as the surface of the pouring block and near the cooling water pipe, also attracts the attention of engineers [25, 26]. Therefore, it is necessary to study the selection method of temperature measurement points in concrete thermal parameter inversion to improve the accuracy of inversion results.

In this study, a two-stage thermal parameters inversion method for a concrete dam based on optimal temperature measuring point selecting was proposed. The first stage is to select the optimal temperature measurement point, and the second stage is to invert the thermal parameters based on the monitoring data from the above measurement points. And then, taking a concrete arch dam as an example, the optimal temperature measuring points required was selected by the proposed method, and the thermal parameters such as thermal diffusivity, adiabatic temperature rise, and surface heat exchange coefficient were inverted. Finally, the accuracy and efficiency of the method was verified.

The paper is organized as follows: Section 2 introduces the selection principle of optimal temperature measurement point for thermal parameter inversion, and the evaluation index and calculation method are determined. Section 3 introduces the inversion principle of concrete thermal parameters and the inversion model is constructed. Section 4 introduces the engineering background, data acquisition, datasets generation, and finite element modeling. Sections 5 and 6 verify the validity of the proposed methods and draw some main conclusions, respectively.

2. Selection Method of Optimal Measuring Point for Thermal Parameters Inversion

2.1. Selection Principle of Optimal Temperature Measuring Point. For the thermal parameters' inversion of concrete, the relationship between the monitoring temperature η_k and the inversion parameters β_i can be expressed as follows [27]:

$$\eta_k = f_k(\beta_1, \beta_2, \cdots, \beta_m). \quad (1)$$

Taking the concrete thermal parameters of the true value for $\beta^* = (\beta_1^*, \beta_1^*, \cdots, \beta_m^*)$ as the benchmark parameter values, and setting the benchmark monitoring quantity as η_k^*, it can be written as follows:

$$\eta_k^* = f_k(\beta_1^*, \beta_2^*, \cdots \beta_m^*). \quad (2)$$

Equation (1) is always established when the parameter β_i varies within its range. The right side of equation (1) is transformed into a Taylor expansion at the reference parameter value as follows:

$$\eta_k = f_k\left(\beta_1^*, \beta_2^*, \cdots \beta_m^*\right) + \sum_{i=1}^{m} S_{ki}\left(\beta_i - \beta_i^*\right), \tag{3}$$

where, S_{ki} is the sensitivity coefficient of the parameter β_i, characterizing the sensitivity of temperature response at a certain location to parameter disturbance; $S(\beta_i)$ can be denoted as follows:

$$S(\beta_i) = \frac{\partial \eta(\beta)}{\partial \beta_i}. \tag{4}$$

The monitoring error and the inversion error are given by $\delta\eta_k = \eta_k - f_k(\beta_1^*, \beta_2^*, \cdots \beta_m^*)$ and $\delta\beta_i = \beta_i - \beta_i^*$. Equation (3) can be written as follows:

$$\delta\eta_k = \sum_{i=1}^{m} S_{ki}\delta\beta_i. \tag{5}$$

Equation (4) can be used to approximately represent the relation between the monitoring error and the inversion error. Therefore, according to the monitoring temperature in the construction site, the system matrix of the concrete thermal parameters is as follows:

$$\delta\boldsymbol{\eta} = \mathbf{S}\delta\boldsymbol{\beta}, \tag{6}$$

where $\delta\eta_k = \eta_k - f_k(\beta_1^*, \beta_2^*, \cdots \beta_m^*), \delta\beta_i = \beta_i - \beta_i^*$, and $\mathbf{S}$ is the sensitivity coefficient matrix.

We obtained the norm from both sides of equation (6) as follows:

$$\|\delta\boldsymbol{\beta}\| \geq \frac{1}{\|\mathbf{S}\|}\|\delta\boldsymbol{\eta}\|. \tag{7}$$

It can be seen from equation (7) that, when the monitoring error is constant, the more significant temperature response at a certain location caused by parameters disturbance, that is, the larger the sensitivity coefficient is, the smaller inversion error based on the temperature monitoring information of the location would be. On the contrary, the smaller the sensitivity coefficient is, the larger error of inversion error will be. Adding the influence of error propagation, too small temperature response may even lead the inversion results to deviate from the actual.

Therefore, this paper took sensitivity coefficient as the key index for selecting the optimal temperature measuring point, and select the measuring point with the largest sensitivity coefficient for thermal parameter inversion.

2.2. Calculation of Sensitivity Coefficient. On the basis of the principle described in "Selection Principle of Optimal Temperature Measuring Point," how to calculate the sensitivity coefficient is a key issue to be solved. Since the three-dimensional (3D) temperature field of the pouring block is highly nonlinear, it is difficult to establish the temperature

response model by analytical method. In this study, establishing temperature simulation model by FEM, and the improved Morris method [28] was used to calculate the sensitivity coefficient as follows:

$$S = \frac{1}{q-1}\sum_{j=1}^{q-1}\frac{\left|Y_{j+1} - Y_j\right|/Y_0}{\left(P_{j+1} - P_j\right)/100}, \tag{8}$$

where Y_0 is the output value of the input reference parameter, P_j is the percentage of the parameter variation of the jth input of the calculation model relative to the reference parameter, and q is the number of times the model runs.

In order to unify the magnitude of the sensitivity coefficient, normalization is carried out as follows:

$$S' = \frac{S - S_{\min}}{S_{\max} - S_{\min}}, \tag{9}$$

where S' is the normalized sensitivity coefficient.

2.3. Determination of Dam Temperature Field. According to the analysis in "Calculation of Sensitivity Coefficient," the temperature field calculation model needs to reflect the temperature difference at different positions to realize the sensitivity analysis of the whole concrete pouring block. Since concrete dams generally adopt water pipe cooling (Figure 1), obviously, the equivalent algorithm [20] of homogenizing water cooling into a whole negative heat source is no longer applicable. Taking into account the model analysis accuracy and modeling efficiency, the heat-fluid coupling algorithm [29] is selected for simulating the temperature field of concrete containing cooling water pipes.

According to the heat conduction theory, an unstable temperature field T is governed by the following differential equation:

$$\frac{\partial T}{\partial t} = a\left(\frac{\partial^2 T}{\partial x^2} + \frac{\partial^2 T}{\partial y^2} + \frac{\partial^2 T}{\partial z^2}\right) + \frac{\partial\theta}{\partial t}, \tag{10}$$

where T is the concrete temperature, t is the time, a is the concrete thermal conductivity, and θ is the adiabatic temperature rise of concrete.

The boundary conditions for equation (10) are as follows:

$$T = T_s,$$

$$\frac{\partial T}{\partial n} = -h_f\left(T_f - T_s\right), \tag{11}$$

$$T(0, t) = T_0(t),$$

where T_s is the concrete temperature of the cooling pipe surface, n is the normal outside direction of the concrete surface, h_f is the convective heat transfer coefficient, T_f is the water temperature around concrete, and T_0 is the water temperature at a pipe inlet.

The heat-fluid coupling algorithm is often used to simulate the arrangement of a water pipe and the variation of water temperature, from which the accurate temperature
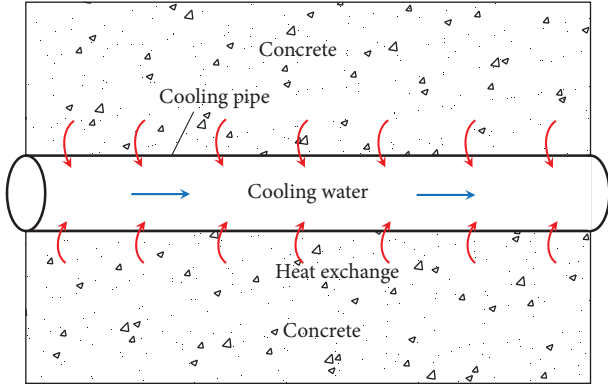
FIGURE 1: Heat exchange between cooling water and concrete.

field can be obtained without encrypting the finite element grid near the water pipe. The concrete and the cooling water pipe in the concrete were simulated by solid elements and heat-fluid pipe elements, respectively. The convection heat transfer between the cooling water and the concrete is simulated by coupling the additional nodes of the heat-fluid pipe element with the concrete element nodes. The heat-fluid coupling element is shown in Figure 2. Compared with the equivalent algorithm, the heat-fluid coupling algorithm could accurately simulate the temperature gradient of the concrete near the cooling pipe, and it could simulate the arrangement of the water pipe and the water temperature within the water pipe, which was more in line with the actual cooling process.

3. Inversion Method of Concrete Thermal Parameters

3.1. Inversion Principle. The iterative inversion method for thermal parameters involves the continuous modification of the thermal parameters through a certain strategy. When the temperature calculated value and the monitored value are fitted optimally, the corresponding parameters are the thermal parameters to be inverted. This method has transformed parameter inversion into a nonlinear optimization problem. The objective function of optimization can be expressed as follows:

$$F = \sum_{i=1}^{p} \sum_{j=1}^{q} \left| \frac{T_{ij} - T_{ij}^{F}}{T_{ij}} \right|, \tag{12}$$

where F is the objective function value, i is the number of temperature measuring points, j is the number of monitoring time series, T^{F} is the temperature calculated temperature, T is the monitored temperature, p and q are the total number of monitoring points and the total number of monitoring times.

3.2. Inversion Model Construction. In iterative inversion, it would be time-consuming and inefficient to repeatedly invoke the finite element subroutine directly for

optimization. To solve this problem, surrogate model is used as an effective alternative in this regard [30]. The core idea of this approach is as follows: first, a small number of expensive finite element simulations are performed to obtain the modeling samples. Then, an approximate mapping model between model inputs and outputs is constructed based on samples, as mentioned. Finally, the optimization algorithm is used to invoke the model to search for the optimal solution.

Whether the inversion can achieve good results or not mainly depends on the performance of the surrogate model. Over the past few decades, several surrogate models have been most widely used, including support vector regression (SVR) [31], kriging (KRG) [32], and radial basis function (RBF) [33]. By comparing different models, the results show that SVR has some advantages in terms of sparsity, accuracy, and flexibility, especially in dealing with small samples and nonlinear problems. In addition, the quality of the inversion results is also related to the optimization method. A variety of optimization algorithms, such as artificial bee colony (ABC) [34], PSO [35], gray wolf optimization (GWO) [36], GA [37], whale optimization algorithm (WOA) [38], and bat algorithm (BA) [39], applied in the model parameter identification have shown good adaptability. Compared with other methods, PSO has the characteristics of simple implementation, wide application, and strong global search capability. Therefore, this paper combined these two to construct a concrete thermal parameters inversion model.

Before establishing the SVR-PSO inversion model, the combination scheme of thermal parameters should be determined first. It is input into a finite element model to obtain the corresponding temperature response, which is applied to the follow-up inversion of the thermal parameters. To reduce the calculating works of the numerical simulation, the uniform design method [40] is introduced to design the combination scheme of thermal parameters, which will significantly reduce the numerical computational workload.

The inversion process based on SVR-PSO is shown in Figure 3, and the steps are as follows:

(1) Generating training sample parameter combination schemes using uniform designs and randomly generating a small number of test sample parameter combination schemes;

(2) Input the sample combination in (1) one by one into the finite element model of the temperature field, and obtain the calculated temperature. Based on the calculated temperature and the monitored temperature at that point, the objective function value is calculated using equation (12);

(3) Take the parameter samples as input and the objective function values as output, the SVR model is trained and validated to obtain a surrogate model between the thermal parameters and the objective function;
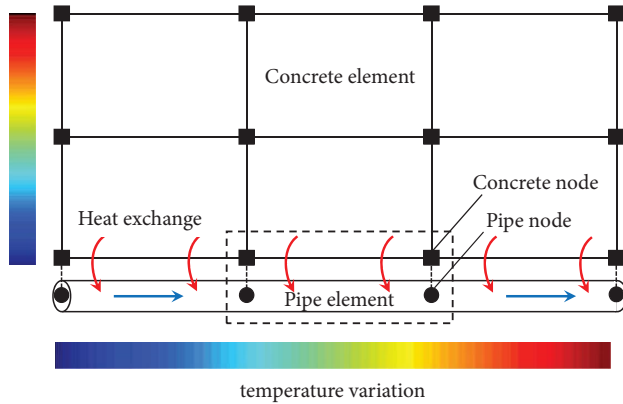
Figure 2: Heat-fluid coupling element.

(4) Use the PSO algorithm to search the feasible domain of the parameters and the trained SVR model to calculate the objective function. When the value of the objective function reaches the minimum, the sets of parameters are the optimal solution to be inverted.

4. Method and Materials

4.1. Project Background. The Baihetan arch dam is located in the lower reach of the Jinsha River, Sichuan Province, in Southwest China, as is shown in Figure 4. It is a concrete double curvature arch dam with a maximum height of 289 m and a total concrete volume of 8.03 million m³. The superhigh arch dam has the characteristics of a huge scale, complex structure, and high quality requirements. In addition, the dam is located in a dry-hot valley area, where the temperature difference between day and night is large, the solar radiation is strong, and the environmental conditions of dam construction are relatively harsh, which poses challenges to the temperature control and crack prevention of the dam concrete.

To prevent temperature cracks, the dam uses low-heat cement concrete. Compared with medium-heat cement, low-heat cement has the advantages of a slow heat release rate in the early stage and low total heat of hydration. The performance of this concrete in the late stage is close to or better than that of medium-heat Portland cement, which can improve the crack resistance of mass concrete. However, the early strength development of low-heat cement concrete is slower, and this concrete's temperature control and crack prevention at an early age have become the focus of engineers. Therefore, it is necessary to invert the concrete thermal parameters of the early age under actual pouring conditions to provide basic simulation parameters for cracking risk analysis.

The temperature monitoring data of a pouring block was selected for inversion. Its thickness is 3 m, and two layers of cooling water pipes were arranged inside. Distributed temperature sensing optical fiber was embedded in the pouring block to monitor the concrete temperature [41]. The technical specifications of the temperature sensing system are shown in Table 1. The distributed optical fiber arrangement and temperature measuring points distribution

are shown in Figure 5. It can be seen that the measuring points 1–9 are located in the middle of the two layers of cooling water pipes to monitor the internal temperature of the pouring block. The no. 1 point was 3 m away from the upstream surface, and the distance between the no. 1–9 points was 1 m. The measuring points 10–13 are located within 0.4 m of the top surface of the pouring block, and they are 0.1 m, 0.2 m, 0.3 m, and 0.4 m, respectively, from the top surface of the pouring block to monitor the surface temperature.

4.2. Inversion Parameters Determination. The commonly used thermal parameters include thermal conductivity λ, thermal diffusivity a, adiabatic temperature rise θ, concrete density ρ, specific heat c, surface heat release coefficient β, and temperature rise law n. The concrete density ρ and the specific heat c can be obtained accurately by experiment. The coefficient of thermal conductivity λ can be determined with the formula $a = \lambda/c\rho$. In this study, the hyperbolic equation was used to express the adiabatic temperature rise and the adiabatic temperature rise θ, and the temperature rise law n had to be inversed. After the completion of the concrete pouring, cooling water and the curing of the storehouse surface were required. At this time, the heat exchange between the concrete and the outside world needed to be expressed by the equivalent surface heat exchange coefficient of the air-concrete β and the water-concrete β'.

In summary, the parameters a, θ, n, β, and β' were chosen as the inversion parameters. The approximate range of each parameter was determined according to literature [16]: $a \in [0.0017, 0.0050]\mathrm{m}^2/h$, $\theta \in [20, 30]°\mathrm{C}$, $\beta \in [10, 60]\mathrm{kj}/(\mathrm{m}^2 \cdot \mathrm{h} \cdot °\mathrm{C})$, $n \in [1.5, 3.5]$, and $\beta' \in [200, 1400]\mathrm{kj}/(\mathrm{m}^2 \cdot \mathrm{h} \cdot °\mathrm{C})$.

4.3. Combination Scheme Design of Multiple Thermal Parameters. Based on the parameter value range determined in Section 4.2, multiple combination schemes of parameters should be designed for the subsequent calculation of temperature response and objective function values. According to the principle of uniform design, the number of levels is generally taken as 3 to 5 times the number of factors, which is determined as 50 in this paper in order to further make the test points evenly scattered. The uniform design table $U_{50}(50^5)$ given in Table 2 is used for training sample input. In addition, 10 sets of parameter combination schemes were randomly generated as test sample inputs, as shown in Table 3.

4.4. Finite Element Modeling. One dam monolith was selected to establish the finite element model. The coordinates were the X-axis in the transverse direction, Y-axis in the downstream direction, and Z-axis in the vertical direction. The heat-fluid coupling algorithm was used to simulate the water pipe cooling, as shown in Figure 6. The total numbers of the nodes, elements, and cooling pipe elements were 22473, 17118, and 3438, respectively. In order to reflect the temperature gradient of the top surface concrete, a dense
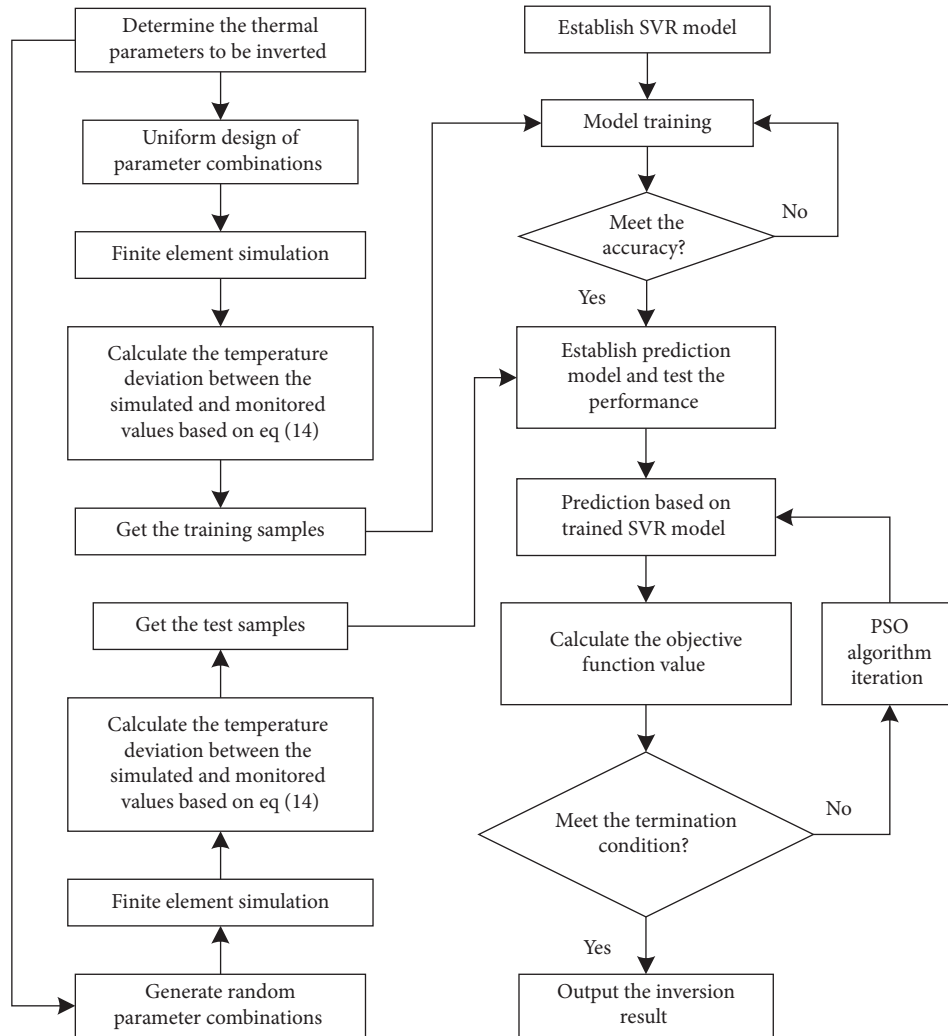
Figure 3: The inversion process based on SVR-PSO.

Figure 4: Construction site.

finite element mesh was divided on the top surface. The material parameters are shown in Table 4, and the cooling water pipe parameters are shown in Table 5. The side, up-stream, downstream, and top surfaces of the pouring block were assumed to be the third type of heat transfer boundary. And the heat exchange between the surface of the pouring block and the cooling water pipe were reflected by the equivalent surface heat release coefficient.

5. Results and Discussion

5.1. Selection of Optimal Temperature Measurement Points. The optimal temperature measurement points used for the thermal parameter inversion were selected using the method proposed in this paper. First of all, a set of reference values was determined by referring to the thermal parameters of several typical dam concrete given in literature [16]. Then, the reference parameters were proportionally disturbed one by one, as shown in Table 6, and the sensitivity coefficient was calculated using equation (8). In sensitivity analysis, the construction parameters are shown in Table 7. Figure 7 shows the sensitivity coefficient contour of each thermal parameter in the section.

As can be seen from Figure 7, due to the limited in-fluence range of external air temperature and water cooling, the deep temperature of pouring block is mainly affected by cement hydration heat and cooling water. The sensitivity of temperature response of deep concrete is greater than shallow when θ, n, and β' were disturbed. The temperature of shallow concrete is significantly affected by air temperature, and the degree of influence gradually decreases with the

TABLE 1: Technical specifications of the temperature sensing system.

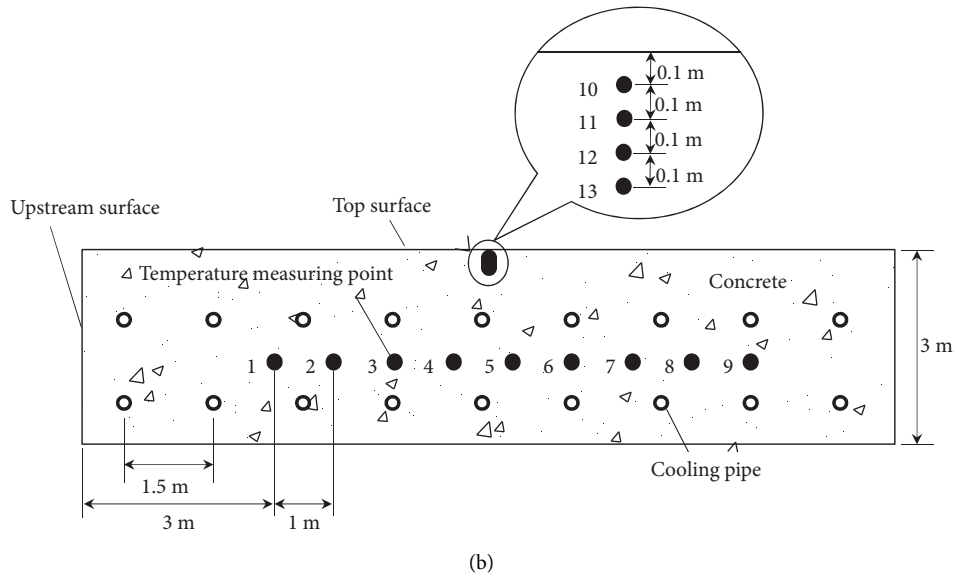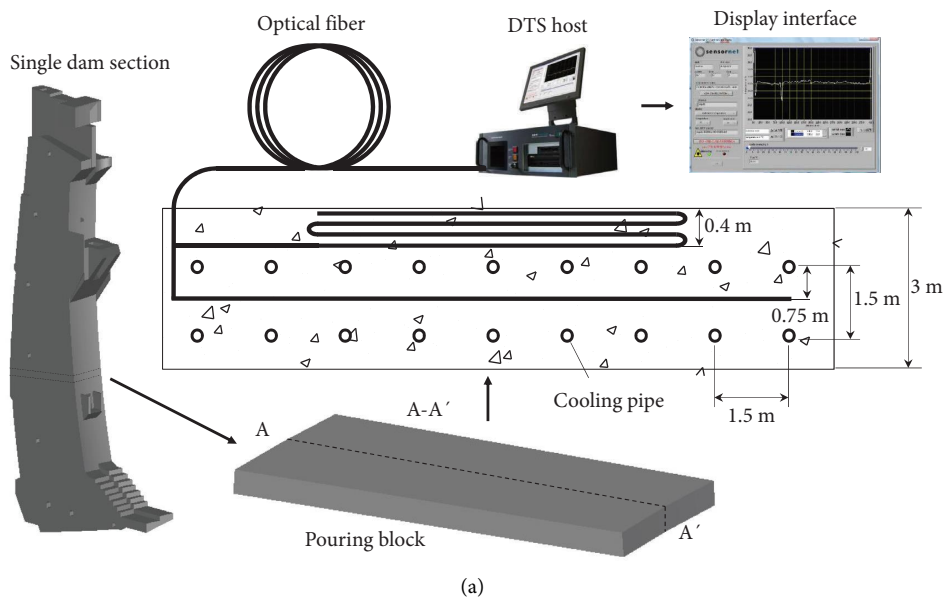| Technical index	Technical specification
Temperature resolution (°C)	0.02
Measurement accuracy (°C)	1
Spatial resolution (m)	1.02
Acquisition frequency	Every 2 hours
Optical fiber type	Multimode fiber (50/125 μm)

(a)

(b)

FIGURE 5: Temperature measuring points distribution. (a) Embedding scheme of temperature measuring optical fiber. (b) Distribution of temperature measuring points.

increase of depth, when β was disturbed, the temperature response sensitivity of shallow concrete was greater than deep. Compared with deep concrete, the heat flow of shallow concrete is more intense. When a was disturbed, the temperature response sensitivity of shallow concrete was greater than deep. The above shows that the thermal characteristics

of concrete have an obvious spatial effect, resulting in different responses of temperature at different spatial locations to the disturbance of each thermal parameter.

The calculation results of the sensitivity coefficients of the above 13 temperature measuring points are shown in Table 8. According to the principle of optimal measurement

TABLE 2: Training sample input.

Number	Parameter θ (°C)	Parameter n	Parameter a (m²/h)	Parameter β [kj/(m²·h·°C)]	Parameter β' [kj/(m²·h·°C)]
1	20.0	2.28	0.1086	53.9	493.9
2	20.2	3.09	0.0955	46.7	812.2
3	20.4	1.83	0.0824	39.6	1130.6
4	20.6	2.64	0.0694	32.4	200.0
5	20.8	3.46	0.0563	25.3	518.4
6	21.0	2.19	0.0433	18.2	836.7
7	21.2	3.01	0.1135	11.0	1155.1
8	21.4	1.74	0.1004	55.9	224.5
9	21.6	2.56	0.0873	48.8	542.9
10	21.8	3.38	0.0743	41.6	861.2
11	22.0	2.11	0.0612	34.5	1179.6
12	22.2	2.93	0.0482	27.3	249.0
13	22.4	1.66	0.1184	20.2	567.3
14	22.7	2.48	0.1053	13.1	885.7
15	22.9	3.30	0.0922	58.0	1204.1
16	23.1	2.03	0.0792	50.8	273.5
17	23.3	2.85	0.0661	43.7	591.8
18	23.5	1.58	0.0531	36.5	910.2
19	23.7	2.40	0.0400	29.4	1228.6
20	23.9	3.21	0.1102	22.2	298.0
21	24.1	1.95	0.0971	15.1	616.3
22	24.3	2.77	0.0841	60.0	934.7
23	24.5	1.50	0.0710	52.9	1253.1
24	24.7	2.32	0.0580	45.7	322.4
25	24.9	3.13	0.0449	38.6	640.8
26	25.1	1.87	0.1151	31.4	959.2
27	25.3	2.68	0.1020	24.3	1277.6
28	25.5	3.50	0.0890	17.1	346.9
29	25.7	2.23	0.0759	10.0	665.3
30	25.9	3.05	0.0629	54.9	983.7
31	26.1	1.79	0.0498	47.8	1302.0
32	26.3	2.60	0.1200	40.6	371.4
33	26.5	3.42	0.1069	33.5	689.8
34	26.7	2.15	0.0939	26.3	1008.2
35	26.9	2.97	0.0808	19.2	1326.5
36	27.1	1.70	0.0678	12.0	395.9
37	27.3	2.52	0.0547	56.9	714.3
38	27.6	3.34	0.0416	49.8	1032.7
39	27.8	2.07	0.1118	42.7	1351.0
40	28.0	2.89	0.0988	35.5	420.4
41	28.2	1.62	0.0857	28.4	738.8
42	28.4	2.44	0.0727	21.2	1057.1
43	28.6	3.26	0.0596	14.1	1375.5
44	28.8	1.99	0.0465	59.0	444.9
45	29.0	2.81	0.1167	51.8	763.3
46	29.2	1.54	0.1037	44.7	1081.6
47	29.4	2.36	0.0906	37.6	1400.0
48	29.6	3.17	0.0776	30.4	469.4
49	29.8	1.91	0.0645	23.3	787.8
50	30.0	2.72	0.0514	16.1	1106.1

TABLE 3: Test sample inputs.

Number	Parameter θ (°C)	Parameter n	Parameter a (m²/h)	Parameter β [kj/(m²·h·°C)]	Parameter β' [kj/(m²·h·°C)]
1	28.1	1.82	0.0925	52.4	726.5
2	29.1	3.44	0.0429	11.9	657.9
3	21.3	3.41	0.1079	26.6	1118.6
4	29.1	2.47	0.1147	12.8	1154.2
5	26.3	3.10	0.0943	15.8	424.2
6	21.0	1.78	0.1006	59.4	787.7
7	22.8	2.34	0.0995	51.7	734.7
8	25.5	3.33	0.0714	29.0	975.6
9	29.6	3.08	0.0924	67.0	1051.2
10	29.6	3.42	0.0537	12.1	1105.6

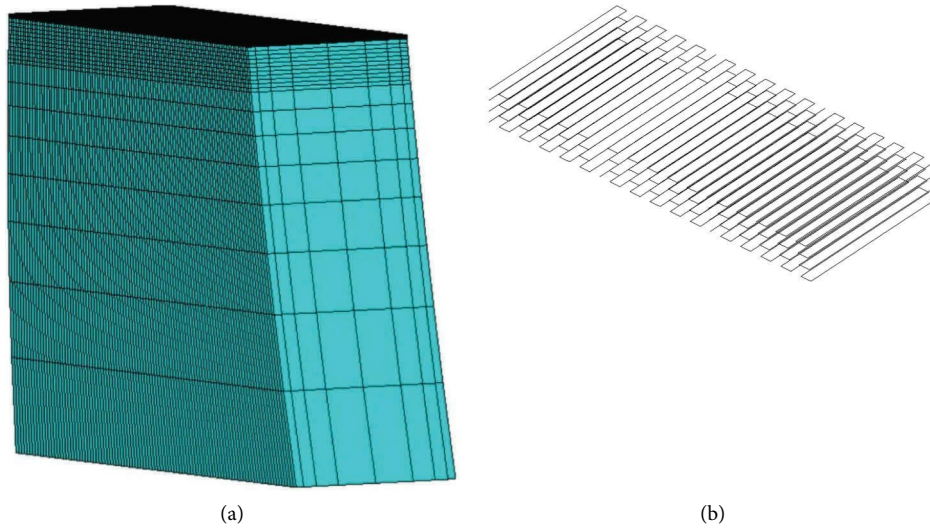FIGURE 6: Finite element model. (a) Dam model. (b) Cooling pipe model.

TABLE 4: Material parameters.

Materials	Concrete	Cooling water
Density (kg/m³)	2601	1000
Specific heat [kj/(kg·°C)]	0.851	4.187

TABLE 5: Parameters of the cooling water pipe.

Inner radius (m)	Outer radius (m)	Arrangement distance (m)
0.014	0.016	1.5×1.5

point selection, the temperature measuring points for the inversion of thermal parameters were determined as no. 1, no. 9, no. 10, and no. 13.

5.2. Inversion Results

5.2.1. Comparison of Different Inversion Model.
The parameter combinations generated in Section 4.3 were input to the finite element model to obtain the training and test sample outputs, and then, the SVR-PSO inversion model was constructed. Since the kernel function of SVR plays a significant role in the whole regression and prediction process, studies have proved that RBF kernel can solve such nonlinear problems well [31], so it was chosen in this paper, and the optimal hyper-parameters were searched by using PSO. Parameters of PSO were set as follows: iteration population was 40, the maximum number of iterations was 100, inertia weight was 7.28, acceleration factors were 2.8 and 1.3, respectively.

Meanwhile, the BPNN-GA inversion model was constructed for comparison. After repeated trial calculation, the number of nodes of the BP neural network was taken as 3, and the better network model was retained by multiple training tests. Parameters of GA were set as follows: population size was 40, the maximum number of iterations was 100, crossover probability was 0.4, and mutation probability was 0.6.

The mean absolute percentage error (MAPE) was also introduced to quantify the effectiveness of the inversion model, where smaller errors indicate a more valid model. It is expressed as follows:

$$\text{MAPE} = \frac{100\%}{n} \sum_{i=1}^{p} \left| \frac{T_i - T_i^F}{T_i} \right|, \tag{13}$$

where n is the number of samples.

TABLE 6: Parameter disturbance range.

Disturbance range (%)	Parameter θ (°C)	Parameter n	Parameter a (m²/h)	Parameter β [kj/(m²·h·°C)]	Parameter β' [kj/(m²·h·°C)]
−30	18.0	2.10	0.0580	29.2	583.3
−20	20.0	2.40	0.0650	33.3	666.7
−10	22.0	2.70	0.0720	37.5	750.0
0	24.0	3.00	0.0800	41.7	833.3
10	26.0	3.30	0.0880	45.8	916.7
20	28.0	3.60	0.0960	50.0	1000.0
30	30.0	3.90	0.1040	54.2	1083.3

TABLE 7: Construction parameters.

Start pipe cooling age (d)	Water flow rate (L/ min) 0~8d	Water temperature (°C) >8d	Pouring temperature (°C)	Pouring time interval (d)
0	25 10	10 14	12	10
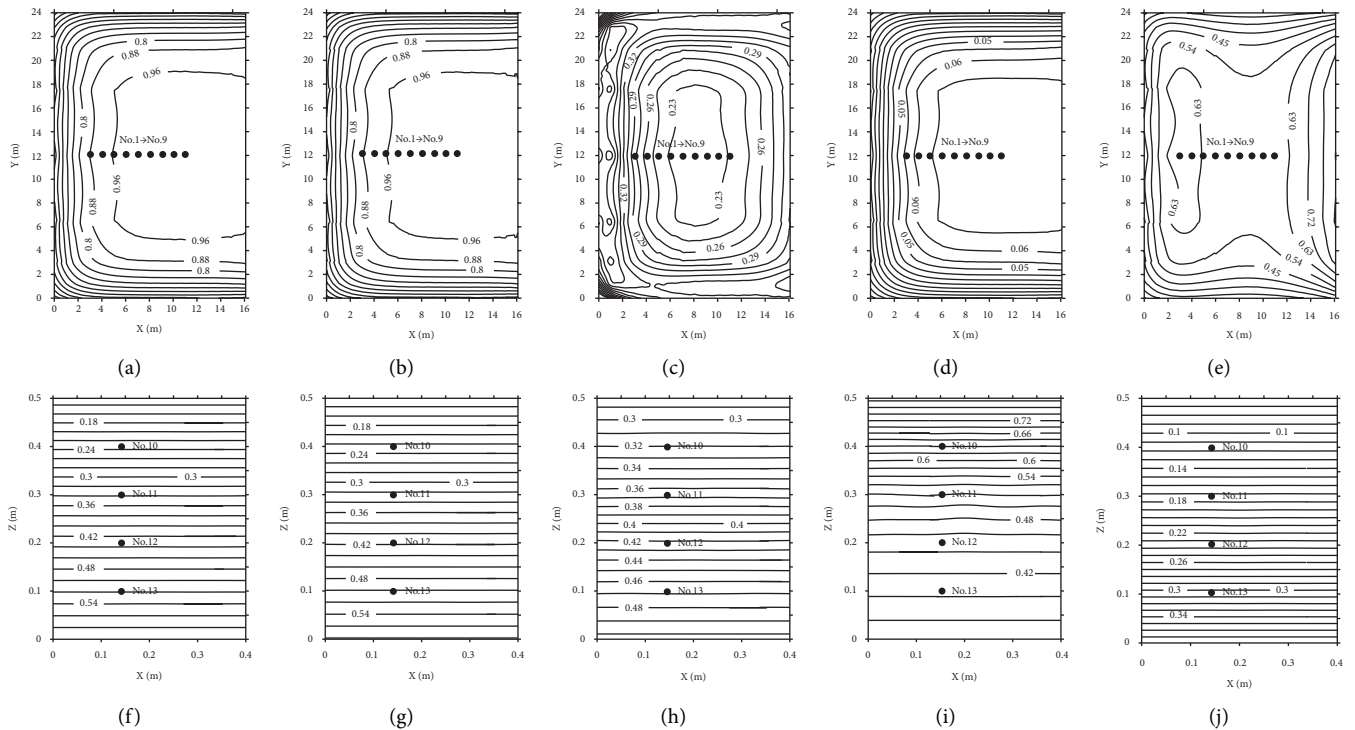
FIGURE 7: Sensitivity coefficient contour. (a)–(e) Show the parameter θ, n, a, β, and β' inside the pouring block, respectively. (f)–(j) Show the parameter θ, n, a, β, and β' on the top surface of pouring block, respectively.

Figure 8 shows the comparison of SVR and BP training and testing results.

As can be seen from Figure 8, both SVR and BP models have shown certain prediction capabilities. In terms of the variation trend, the SVR model has better fitting than the BP model. The training and testing errors of the BP model are 5.20% and 17.68%, respectively, while the SVR model is 0.81% and 8.00%, which is 84.42% and 54.75% lower than the former, respectively. It indicates that the SVR model can better describe the small sample spatial information than the BP model. However, the training and test samples are only a

small part of the space, and their prediction results prove that the training model may be good. In this paper, we focus on comparing the generalization effect of the two models. In this paper, the focus is on comparing the inversion errors of the two models.

The inversion of the thermal parameters was performed using the above two models. The evolution lines of the two models are shown in Figure 9. It is clear that SVR-PSO converges earlier and has higher search efficiency. The final convergence value of BPNN-GA is close to 0, which is almost impossible for the existence of finite element modeling

TABLE 8: Sensitivity calculation results.

Measuring point number	Sensitivity coefficient				
	Parameter θ	Parameter n	Parameter a	Parameter β	Parameter β'
1	0.984	0.978	0.215	0.066	0.775
2	0.991	0.986	0.229	0.068	0.678
3	0.993	0.989	0.222	0.068	0.624
4	0.995	0.992	0.217	0.068	0.568
5	0.997	0.995	0.214	0.068	0.532
6	0.999	0.997	0.215	0.068	0.514
7	0.999	0.998	0.216	0.068	0.511
8	0.999	0.998	0.219	0.068	0.526
9	1.000	1.000	0.228	0.069	0.540
10	0.233	0.225	0.321	0.642	0.116
11	0.341	0.328	0.359	0.496	0.171
12	0.436	0.420	0.430	0.446	0.233
13	0.518	0.501	0.467	0.405	0.306
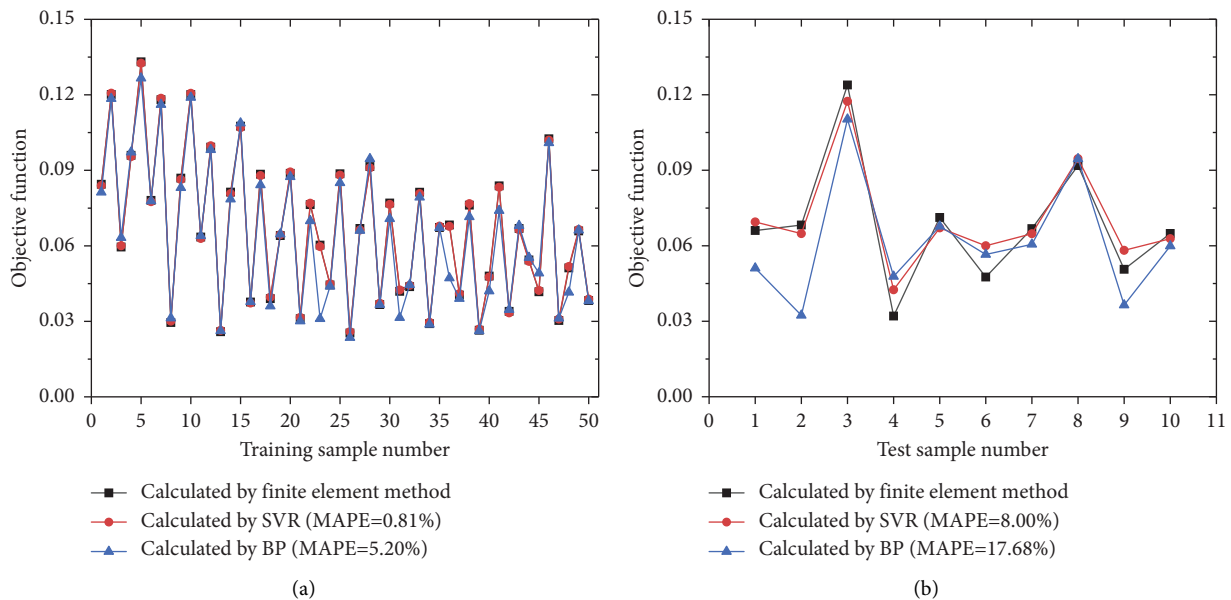
FIGURE 8: Comparison of SVR and BP training and testing results. (a) Training samples. (b) Test samples.

simplification and monitoring errors, again proving that the BP model has a greater error in the sample space of this paper.

The inversion results of the two models are shown in Table 9. Since the actual parameters in the project are unknown, the inversion result cannot be compared with the real value. In this paper, the calculated temperature based on the inversion result is compared with the monitored temperature, and MAPE is used to evaluate the accuracy of the inversion result.

The above thermal parameters were input to the temperature field simulation program, and the calculated temperature and the measured temperature were compared to verify the accuracy and reliability of the parameters, as shown in Figure 10. The comparison of MAPE for all measurement points is shown in Figure 11.

As shown in Figure 10, in general, the temperature calculated based on SVR-PSO model inversion results is closer to the monitored values, while the BPNN-GA model is slightly less effective. The MAPE for the four measurement points corresponding to the SVR-PSO model was 4.40%, 4.14%, 2.06%, and 1.50%, and the BPNN-GA model was 5.14%, 4.11%, 4.14%, and 2.79%, respectively.

As can be seen from Figure 11, the accuracy of the SVR-PSO model is generally better than that of the BPNN-GA model, and their average MAPE at all measurement points are 2.65% and 3.71%, respectively, with the former being 28.54% lower than the latter. It indicates that the inversion accuracy of the SVR-PSO model is higher than the BPNN-GA model in the sample space in this paper.

In addition, it can be seen in Figure 11 that the MAPE of measurement points no.1–9 corresponding to both models is
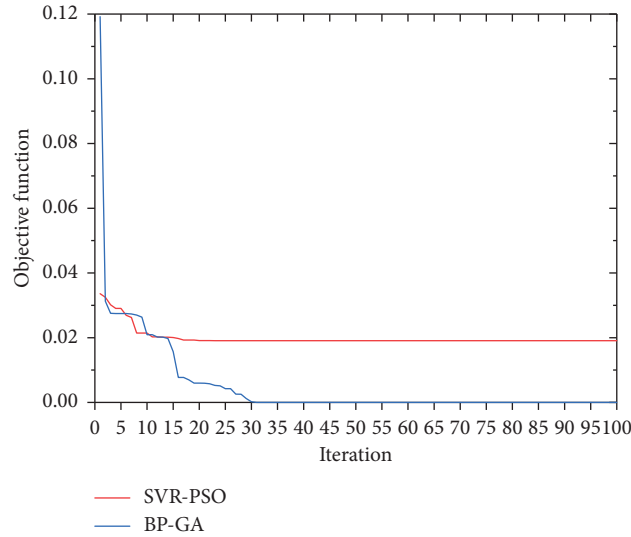
Figure 9: The evolution line of objective function value.

Table 9: Inversion results.

Inversion model	Parameter θ (°C)	Parameter n	Parameter a (m²/h)	Parameter β [kj/(m²·h·°C)]	Parameter β' [kj/(m²·h·°C)]
SVR-PSO	25.9	2.00	0.0032	25.6	1152.7
BPNN-GA	24.4	1.67	00044	10.3	356.3

smaller than that of points no. 10–13. The main reason for this was that the temperature of the surface measurement point (no. 10–13) was greatly affected by random factors such as the ambient temperature, solar radiation, and maintenance measures, which were difficult to consider accurately in the calculation.

5.2.2. Comparison of Inversion Results Based on Different Measurement Points. To further verify the effectiveness of the proposed method, the surface points measuring no. 10–13 were selected (the following was called combination ②), and the thermal parameters were inverted. Compared with the Optimal measuring points: no. 1, no. 9, no. 10, and no. 13 (the following was called combination ①), the temperature of the measuring point for the adiabatic temperature rise θ, the temperature rise law n, and the cooling water pipe equivalent surface heat release coefficient β' sensitivity coefficient were smaller. The inversion results based on combination ② were as follows: $a = 0.0028$ m²/h, $\theta = 28.8$°C, $\beta = 51.0$ kj/(m²•h•°C), $n = 1.99$, and $\beta' = 444.9$ kj/(m²•h•°C). The above parameters were input into the temperature field simulation model, and the MAPE was

calculated. The comparison of MAPE for the two combinations is shown in Figure 12.

As shown in Figure 12, the MAPE of two combinations at no. 10–13 measuring points are very close, with the average values of 4.27% and 4.12%, respectively, indicating that the calculation accuracy is close. At no. 1–9 measuring points, MAPE of combination ① was significantly lower than that of combination ②, with average values of 1.93% and 4.12%, respectively. Since the measurement points of combination ② are all surface measurement points, the temperature information monitored mainly reflects the surface temperature characteristics of the pouring block. When some thermal parameters, such as cooling water pipe equivalent surface heat release coefficient, are disturbed, the temperature response of these measuring points is not sensitive. Under the joint influence of monitoring errors, it is difficult for inversion results to reflect the temperature characteristics of the whole pouring block fully. In combination ①, the monitoring information includes the temperature characteristics of different positions of the pouring block, which allows to take into account the temperature response caused by the disturbance of different thermal parameters. The average MAPE of the two combinations at
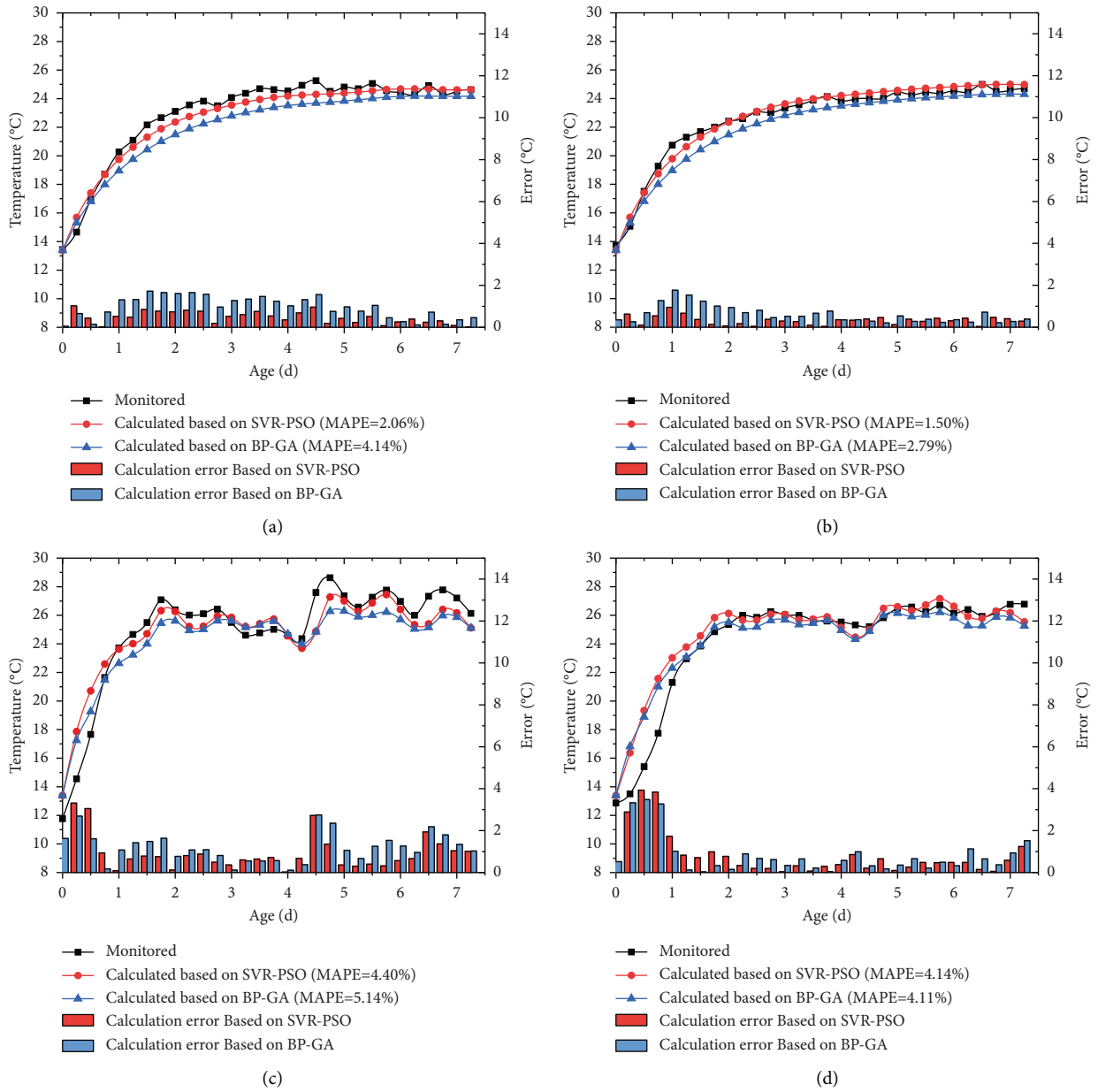
Figure 10: Comparison of the temperature variation. (a) No. 1 point. (b) No. 9 point. (c) No. 10 point. (d) No. 13 point.
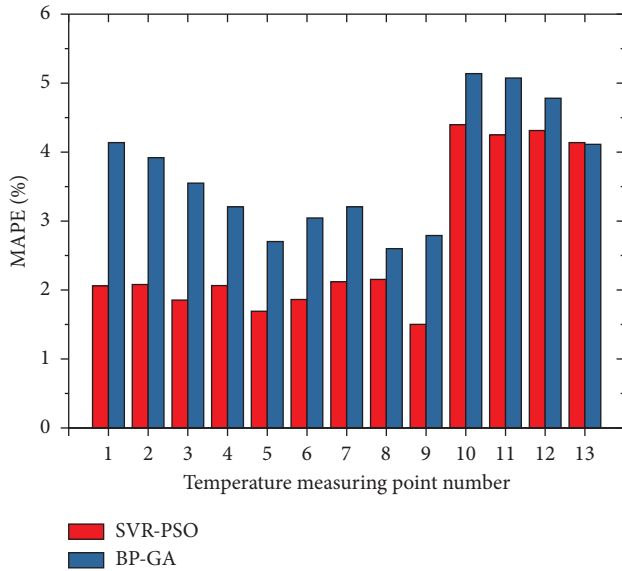
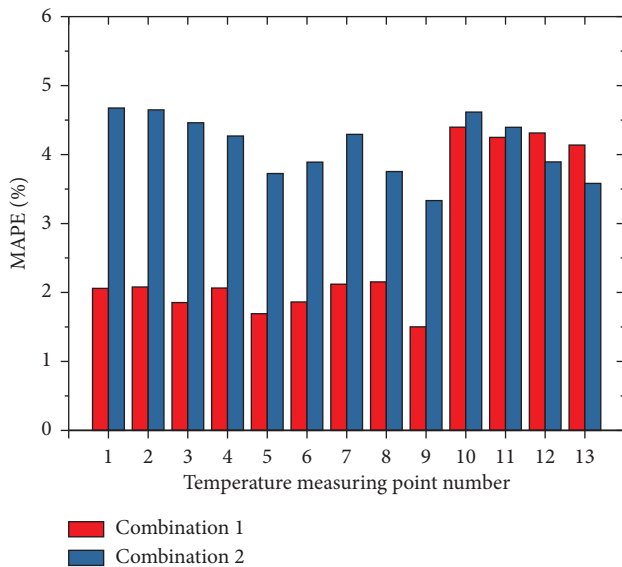FIGURE 11: Comparison of MAPE for two inversion models.

FIGURE 12: Comparison of MAPE for the two combinations.

all measuring points is 2.65% and 4.12%, respectively, and the error based on the optimal measuring point is reduced by 35.57%. Therefore, the temperature field with good overall consistency can be obtained by inversion based on the selection of optimal measuring points, which proves that the proposed method is effective.

6. Conclusions

To improve the inversion accuracy of thermal parameters of dam concrete, a two-stage inversion method based on the selection of optimal temperature measurement points is proposed in this paper. Firstly, the principle, index, and implementation method of selecting the optimal measuring point are studied, which solve the problem on the selection of the optimal

temperature measuring points for thermal parameters inversion in concrete dam. Secondly, based on the optimization method of the surrogate model, the SVR-PSO inversion model is constructed, which can further reduce the calculation cost theoretically. Finally, the proposed method is applied to the thermal parameter inversion of Baihetan Dam concrete. The main conclusions are as follows:

(1) Based on the modeling samples in this paper, SVR is lower than BPNN in both training and testing errors, indicating that SVR has an advantage over BPNN in describing small sample spatial information, which can reduce the workload of numerical simulation in inversion. Importantly, the average error of inversion results based on the SVR-PSO model is 28.54% lower than that of the BPNN-GA model. It shows that the inversion accuracy of the SVR-PSO model is better than that of the BPNN-GA model.

(2) The average error of the inversion results based on the optimal measurement points is 35.57% lower than the nonoptimized ones. It shows that the inversion based on the optimal measurement points can obtain a temperature field with good overall consistency and also proves the effectiveness of the proposed method.

The application examples show that the proposed method is helpful to improve the accuracy of thermal parameters inversion, and can also provide reference for similar projects.

Data Availability

The data used to support the findings of this study are available from the corresponding author upon request.

Conflicts of Interest

The authors declare that there are no conflicts of interest regarding the publication of this paper.

Acknowledgments

References

[1] X. F. Zhang, P. P. Wei, and X. Zhang, "Experimental study on equivalent strength of induced joints with consideration to influence of concrete strength, inducer spacing, and concrete age," *Advances in Civil Engineering*, vol. 2020, Article ID 5187264, 13 pages, 2020.

[2] E. Castilho, N. Schclar, and C. Tiago, "FEA model for the simulation of the hydration process and temperature

evolution during the concreting of an arch dam," *Engineering Structures*, vol. 174, pp. 165–177, 2018.

[3] H. W. Zhou, Y. H. Zhou, and C. J. Zhao, "Optimization of the temperature control scheme for roller compacted concrete dams based on finite element and sensitivity analysis methods," *The Civil Engineering Journal*, vol. 3, pp. 1–16, 2016.

[4] A. A. Abdulrazeg, J. Noorzaei, and P. Khanehzaei, "Effect of temperature and creep on roller compacted concrete dam during the construction stages," *Computer Modeling in Engineering and Sciences*, vol. 68, no. 3, pp. 239–268, 2010.

[5] A. A. Abdulrazeg, J. Noorzaei, and M. S. Jaafar, "Thermal and structural analysis of RCC double-curvature arch dam," *Journal of Civil Engineering and Management*, vol. 20, no. 3, pp. 434–445, 2014.

[6] A. Gaspar, F. Lopez-Caballero, A. Modaressi-Farahmand-Razavi, and A. Gomes-Correia, "Methodology for a probabilistic analysis of an RCC gravity dam construction. Modelling of temperature, hydration degree and ageing degree fields," *Engineering Structures*, vol. 65, pp. 99–110, 2014.

[7] B. F. Zhu, "Effect of cooling by water flowing in nonmetal pipes embedded in mass concrete," *Journal of Construction Engineering and Management*, vol. 125, no. 1, pp. 61–68, 1999.

[8] X. H. Liu, Y. Duan, and W. Zhou, "Modeling the piped water cooling of a concrete dam using the heat-fluid coupling method," *Journal of Engineering Mechanics Asce*, vol. 139, no. 9, pp. 1278–1289, 2013.

[9] S. Qiang, Z. Q. Xie, and R. Zhong, "A p-version embedded model for simulation of concrete temperature fields with cooling pipes," *Water Science and Engineering*, vol. 8, no. 3, pp. 248–256, 2015.

[10] J. Cheng, T. C. Li, and X. Q. Liu, "A 3D discrete FEM iterative algorithm for solving the water pipe cooling problems of massive concrete structures," *International Journal for Numerical and Analytical Methods in Geomechanics*, vol. 40, no. 4, pp. 487–508, 2016.

[11] C. Lim, J. Kim, and T. Seo, "Prediction of concrete adiabatic temperature rise characteristic by semi-adiabatic temperature rise test and FEM analysis," *Construction and Building Materials*, vol. 125, pp. 679–689, 2016.

[12] L. Pei, P. Dai, K. He, Z. Wu, and J. Chen, "Reliability analysis of temperature control of high RCC arch dam," *Advances in Science and Technology of Water Resources*, vol. 36, no. 1, pp. 90–94, 2016.

[13] L. F. Yang, H. Z. Su, and Z. P. Wen, "Improved PLS and PSO methods-based back analysis for elastic modulus of dam," *Advances in Engineering Software*, vol. 131, pp. 205–216, 2019.

[14] Y. J. Chen, C. S. Gu, and B. B. Wu, "Inversion modeling of dam-zoning elasticity modulus for heightened concrete dam using ICS-IPSO algorithm," *Mathematical Problems in Engineering*, vol. 2019, Article ID 9328326, 13 pages, 2019.

[15] S. Shin, S. Park, and J. Kim, "Time-lapse electrical resistivity tomography characterization for piping detection in earthen dam model of a sandbox," *Journal of Applied Geophysics*, vol. 170, Article ID 103834, 2019.

[16] B. F. Zhu, *Thermal Stresses and Temperature Control of Mass Concrete*, China Water & Power Press, Beijing, China, 2012.

[17] J. X. Ding and S. H. Chen, "Simulation and feedback analysis of the temperature field in massive concrete structures containing cooling pipes," *Applied Thermal Engineering*, vol. 61, no. 2, pp. 554–562, 2013.

[18] G. R. Chen and B. Yang, "Back analysis of thermal parameters of mass concrete and its application based on micro-genetic algorithm," *Advanced Materials Research*, vol. 936, pp. 1463–1467, 2014.

[19] L. Pei, J. K. Chen, and Z. Y. Wu, "Response surface genetic algorithm of back analysis of concrete thermal parameters," *Materials Research Innovations*, vol. 19, pp. 840–845, 2016.

[20] H. W. Zhou, Y. H. Zhou, and C. J. Zhao, "Feedback design of temperature control measures for concrete dams based on real-time temperature monitoring and construction process simulation," *KSCE Journal of Civil Engineering*, vol. 22, no. 5, pp. 1584–1592, 2018.

[21] J. S. Ouyang, X. Chen, and Z. Huangfu, "Application of distributed temperature sensing for cracking control of mass concrete," *Construction and Building Materials*, vol. 197, pp. 778–791, 2019.

[22] F. Wang, Y. H. Zhou, and C. J. Zhao, "Inverse analysis of concrete dam thermal parameters based on an improved particle swarm optimization method," *Journal of Vibration and Shock*, vol. 38, no. 12, pp. 168–174, 2019.

[23] Y. Li, L. Nie, and B. Wang, "A numerical simulation of the temperature cracking propagation process when pouring mass concrete," *Automation in Construction*, vol. 37, pp. 203–210, 2014.

[24] Sl 282-2003, *Design Specification for Concrete Arch Dams*, Ministry of Water Resources of the P. R. China, 2003.

[25] P. R. Singh and D. C. Rai, "Effect of piped water cooling on thermal stress in mass concrete at early ages," *Journal of Engineering Mechanics*, vol. 144, no. 3, 11 pages, Article ID 04017183, 2018.

[26] Y. H. Zhou, C. P. Liang, and F. Wang, "Field test and numerical simulation of the thermal insulation effect of concrete pouring block surface based on DTS," *Construction and Building Materials*, vol. 343, p. 17, Article ID 128022, 2022.

[27] Y. G. She, "Principles of optimal measured arrangement and its application for back-analysis in underground engineering," *Journal of China Coal Society*, vol. 36, no. 2, pp. 308–314, 2011.

[28] A. Francos, F. J. Elorza, and F. Bouraoui, "Sensitivity analysis of distributed environmental simulation models: understanding the model behaviour in hydrological studies at the catchment scale," *Reliability Engineering & System Safety*, vol. 79, no. 2, pp. 205–218, 2003.

[29] X. H. Liu, C. Zhang, and X. L. Chang, "Precise simulation analysis of the thermal field in mass concrete with a pipe water cooling system," *Applied Thermal Engineering*, vol. 78, pp. 449–459, 2015.

[30] M. J. G. Rad, S. Ohadi, and J. Jafari-Asl, "GNDO-SVR: an efficient surrogate modeling approach for reliability-based design optimization of concrete dams," *Structures*, vol. 35, pp. 722–733, 2022.

[31] S. L. Ding, C. Fang, and S. L. Zhang, "Comparative study of accurate descriptions of hot flow behaviors of BT22 alloy by intelligence algorithm and physical modeling," *Mathematical Problems in Engineering*, vol. 2021, Article ID 6699514, 17 pages, 2021.

[32] H. W. Xu, X. Zhang, and H. Li, "An ensemble of adaptive surrogate models based on local error expectations," *Mathematical Problems in Engineering*, vol. 2021, Article ID 8857417, 14 pages, 2021.

[33] H. Zou, Q. F. Wu, and Y. G. Zhang, "Research on optimization of structural parameters of equipment cabin bottom cover," *Mathematical Problems in Engineering*, vol. 2022, Article ID 6204795, 13 pages, 2022.

[34] H. B. Zhao and S. D. Yin, "Inverse analysis of geomechanical parameters by the artificial bee colony algorithm and multi-output support vector machine," *Inverse Problems in Science and Engineering*, vol. 24, no. 7, pp. 1266–1281, 2016.

[35] B. W. Liu, Z. W. Wang, and X. Y. Zhong, "Particle swarm optimization algorithm in numerical simulation of saturated rock slope slip," *Mathematical Problems in Engineering*, vol. 2021, Article ID 6682659, 11 pages, 2021.

[36] J. Wang, Y. P. Xu, and C. She, "Optimal parameter identification of SOFC model using modified gray wolf optimization algorithm," *Energy*, vol. 240, p. 10, Article ID 122800, 2022.

[37] X. M. Dong and L. F. Chen, "Parameter identification of 3D elastic-plastic model for tunnel engineering based on improved genetic algorithm," *Mathematical Problems in Engineering*, vol. 2022, Article ID 8305175, 8 pages, 2022.

[38] R. Ni and X. D. Liang, "Seismic inversion problem using a multioperator whale optimization algorithm," *Discrete Dynamics in Nature and Society*, vol. 2022, Article ID 1966054, 14 pages, 2022.

[39] A. Andalib, B. Aminnejad, and A. Lork, "Compressive strength prediction of self-compacting concrete-A bat optimization algorithm based ANNs," *Advances in Materials Science and Engineering*, vol. 2022, Article ID 8404774, 12 pages, 2022.

[40] Y. T. Pang, X. Y. Zhou, and W. He, "Uniform design–based Gaussian process regression for data-driven rapid fragility assessment of bridges," *Journal of Structural Engineering*, vol. 147, no. 4, 15 pages, Article ID 04021008, 2021.

[41] H. W. Zhou, Z. G. Pan, and Z. P. Liang, "Temperature field reconstruction of concrete dams based on distributed optical fiber monitoring data," *KSCE Journal of Civil Engineering*, vol. 23, no. 5, pp. 1911–1922, 2019.